ETH_zürich_

Long-chain hydrocarbons by CO2 electroreduction using polarized nickel catalysts

Journal Article

Author(s):
Zhou, Yansong; Martín Fernández, Antonio José (iD); Dattila, Federico; Xi, Shibo; López, Núria; Pérez-Ramírez, Javier; Yeo, Boon Siang

Long-chain hydrocarbons via CO₂ electroreduction enabled by polarized nickel catalysts

Yansong Zhou[1], Antonio José Martín[2], Federico Dattila[3,4], Shibo Xi[5], Núria López[3]*, Javier Pérez-Ramírez[2]*, Boon Siang Yeo[1]*

[1]*Department of Chemistry, Faculty of Science, National University of Singapore, Singapore*

[2]*Institute for Chemical and Bioengineering, Department of Chemistry and Applied Biosciences, ETH Zürich, Zürich, Switzerland*

[3]*Institute of Chemical Research of Catalonia (ICIQ), The Barcelona Institute of Science and Technology (BIST), Tarragona, Spain*

[4]*Present address: CREST Group, Department of Applied Science and Technology (DISAT), Politecnico di Torino, Turin, Italy*

[5]*Institute of Chemical and Engineering Sciences, A*STAR, Singapore*

*Email: nlopez@iciq.es (NL), jpr@chem.ethz.ch (JPR), chmyeos@nus.edu.sg (BSY)

Abstract: The electroreduction of CO_2, driven by renewable electricity, can be used to sustainably generate synthetic fuels. To date, only copper-based materials can catalyze the formation of multicarbon products, albeit limited to C_2-C_3 molecules. Herein, we disclose that inorganic nickel oxygenate-derived electrocatalysts can generate linear and branched C_3-C_6 hydrocarbons with sustained Faradaic efficiencies up to 6.5%, in contrast with the practically-inactive metallic nickel. *Operando* X-ray absorption spectroscopy, electrochemical CO stripping, and density functional theory (DFT) pinpoint the presence of stable, polarized $Ni^{\delta+}$ active sites associated with Ni-O bonds, which bind to CO moderately. The reduction of selected C_1 molecules and DFT simulations suggest that the $Ni^{\delta+}$ sites promote a mechanism reminiscent of Fischer-Tropsch synthesis: $COOH + CH_x$ coupling followed by successive CH_x insertions. Our results disclose atom polarization as the key that prevents nickel from CO poisoning, and enables it to reduce CO_2 to a wider pool of valuable products.

The electrocatalytic CO_2 reduction reaction (CO_2RR) powered by renewable electricity is a highly appealing method to produce hydrocarbons, as compared to traditional fossil fuel-derived pathways. Multicarbon products are of particular interest since they are ubiquitously used as chemicals and fuels[1]. Due to their mild CO and H binding, copper-based catalysts constitute the only family of materials that can promote C-C coupling with appreciable rates[2]. To date, only C_2 molecules such as ethylene and ethanol have been obtained with remarkable Faradaic efficiencies (*FEs*) and current densities (*j*)[3-6].

Efforts to develop alternative catalysts that can form longer carbon chain products have not been particularly successful. Interestingly, many of those showing measurable activity typically have a common feature, which is the presence of nickel. For example, Ni-Ga alloys yielded *FE* < 2% for ethylene and ethane[7]; nickel phosphides exhibited CO_2RR selectivity towards one C_3 and one C_4 oxyhydrocarbons (methylglyoxal and 2,3-furandiol) at very small overpotentials of 10 mV and with very low current densities[8]. A previous work on metallic nickel using a 60 atm CO_2 feed showed that hydrocarbons containing up to four carbon atoms could be formed, though with modest yields ($FE_{C3+} \sim 1\%$)[9]. The ability of these Ni-based systems to promote C-C coupling is unforeseen, since Hori and co-workers[10] have earlier described the facile CO poisoning of metallic nickel during CO_2RR, which leads to its high activity toward the parasitic hydrogen evolution reaction (HER).

Herein, we disclose that catalysts derived from inorganic nickel oxygenates (INOs), such as nickel phosphate, are unexpectedly active towards CO_2RR with total *FEs* toward carbonaceous products of up to ~30%. Specifically, these reduce CO_2 to hydrocarbons with relevant selectivity (*FE* ~ 16%), among which C_{3+} hydrocarbons stand out. Faradaic efficiencies of 6.5% were achieved for C_3-C_6 hydrocarbon products with partial current densities of $j = 0.91$ mA cm^{-2}, which surpassed the state-of-the-art copper (*FE* = 2.9% and $j = 0.22$ mA cm^{-2} for C_3-C_4 hydrocarbons[11]) or any other known material. Through an interplay

of theory and experiments including *operando* spectroscopy, we demonstrate the presence of $Ni^{\delta+}$ catalytic sites associated with Ni-O bonds that remain stable during CO_2RR. Unlike Ni^0, $Ni^{\delta+}$ sites bind CO moderately, which thus prevents them from being poisoned. The reduction of a series of C_1 molecules, namely CO, formaldehyde, and formic acid further allows us to identify reactive species that we propose to participate in a Fischer-Tropsch-like insertion mechanism for the initiation and propagation of the hydrocarbon chain. The polarization of the Ni sites was found critical for tuning the adsorption strength of the key reaction intermediates, which enables CO_2 reduction to proceed in a sustained fashion without catalyst deactivation. We envision that our discovery of a family of earth-abundant catalysts able to produce long-chain hydrocarbons, through a mechanism distinct from that on copper, could contribute to the global development of a net-zero carbon cycle for producing synthetic fuels.

Results

Catalytic performance of nickel electrocatalysts

The first evidence of the potential of nickel catalysts emerged from the analysis of products formed on a polished metallic Ni disc under ambient conditions. CO_2 was reduced in a H-cell to a variety of C_2-C_5 hydrocarbons with total multicarbon product $FE_{C2+} = 0.3\%$. Remarkably, a Ni disc modified with NiO via electrochemical passivation showed enhanced performance toward multicarbon products with $FE_{C2+} = 0.8\%$ (**Supplementary Figs. 1** and **2**). The ~2.7 times increase in both the selectivity and partial current density for C_{2+} products suggests a denser population of active sites for C-C coupling on the NiO-derived surface (**Supplementary Fig. 3**). Hence, we put forth that electrocatalysts derived from INOs may have a greater potential toward the formation of long-chain hydrocarbons.

To verify this hypothesis, we prepared Ni catalysts by electrochemically reducing a series of INOs supported on carbon black. These are nickel phosphate, nickel carbonate, nickel borate, nickel bicarbonate, nickel hydroxide, and nickel oxide (physico-chemical

characterization of the materials before electrochemical reduction is presented in **Supplementary Figs. 4-6**). Sputter-deposited Ni (s-Ni) was used as a control sample (**Supplementary Figs. 7** and **8**). All electrocatalysts derived from the INOs favored the formation of long-chain hydrocarbons using 0.1 M $KHCO_3$ electrolyte in a flow cell, reaching a total $FE_{C2+, hydrocarbons}$ above 10% on the nickel phosphate-derived catalyst (**Fig 1a** and **Extended Data Table 1**). Additional experiments using non-buffering 0.1 M K_2SO_4 and 0.1 M KOH electrolytes showed decreased performance, suggesting the detrimental effect of highly alkaline local environments arising from the production of OH^- during CO_2RR and HER (**Supplementary Fig. 9**)[12].

The rich chemistry offered by these Ni catalysts is unveiled when we inspect the product distribution - linear and branched hydrocarbons up to C_6 as well as a minor amount of oxygenates including alcohols ($FE_{alcohol} = 3.8\%$) up to C_4 were detected (**Extended Data Table 1**; **Supplementary Figs. 2, 10** and **11**). Isotope-labeled $^{13}CO_2$ experiments confirm the CO_2RR origin of the hydrocarbons (**Supplementary Fig. 10**). We note the outstanding performance toward C_{3+} hydrocarbons ($FE_{C3+, hydrocarbons} = 6.5\%$) at -1.2 V versus reversible hydrogen electrode (RHE). These FE values compare favorably to previously reported systems (**Supplementary Table 1**). All Ni electrocatalysts showed sustained CO_2RR performance over 12 h (**Fig. 1b**, **Supplementary Fig. 12**). After 12 h operation, they were analyzed by scanning electron microscopy (SEM), revealing similar morphologies after operation (**Supplementary Fig. 8**). Despite this promising stability, even longer-term stability tests to address practical industrial requirements will still be required, as these catalysts are further developed towards maturity.

The formation of C_1-C_6 hydrocarbons, including branched ones such as isobutane and isobutene, suggests polymerization of adsorbed C_1 intermediates (CO or CH_x, $x = 1, 2$) resembling Fischer-Tropsch synthesis. Indeed, the parallelism is evident by the product distribution of the hydrocarbons, which follows the Anderson-Schulz-Flory (ASF) model

5

(**Supplementary Figs. 13** and **14**). Long-chain hydrocarbons were more favored on the INO-derived electrocatalysts, as reflected by their chain growth probability values $\alpha > 0.40$, which are higher compared to that of s-Ni ($\alpha = 0.30$). Remarkably, the tendency of INO-derived electrocatalysts to form hydrocarbons increases, compared to metallic Ni, as the carbon chain length grows (**Fig. 1c**).

To explore the influence of morphology on the observed product distributions, we assessed it by SEM and double-layer capacitance measurements and conclude that the morphology of the electrodes could not be used to explain their CO_2RR performance, or the differences in selectivity within the family of INO-derived catalysts (**Supplementary Figs. 8 and 15, Supplementary Table 2**). Analysis of cyclic voltammograms to determine the active Ni electrochemical surface areas (ECSA) enabled the calculation of ECSA-normalized current densities (**Supplementary Fig. 16** and **Supplementary Table 2**), which also reveal that the formation of C_{3+} hydrocarbons cannot be correlated to the surface area of Ni. In view of these results, we embark to investigate the nature of the active sites so as to unravel the main features behind their ability to reduce CO_2 to long-chain hydrocarbons. Given the similar product distribution and performance within the family of INO-derived materials, we chose nickel phosphate-derived electrocatalyst (PD-Ni), the most selective one toward C_{2+} products ($FE_{C2+} = 14.1\%$, including hydrocarbons and oxygenates), for a more extended study (**Extended Data Table 1**).

Before we assess the active sites of PD-Ni, a comparison of the hydrocarbon distributions on PD-Ni and the reference metallic Cu is of utmost relevance. Our literature survey reveals that even the best Cu system exhibited very modest yields toward C_3 hydrocarbons with only trace amounts of C_4 (**Supplementary Tables 1** and **3**). We further compare PD-Ni with a reference nanoparticulated Cu electrode in CO_2-saturated 0.1 M $KHCO_3$ electrolyte at –1.0 V versus RHE, the optimum bias for C-C coupling on copper (**Fig. 2** and

Supplementary Fig. 2)[13]. As expected, Cu produced mainly ethylene ($FE = 16.1\%$), with a trace amount of propylene as the sole detectable C_{3+} hydrocarbon ($FE < 0.1\%$). C_1-C_3 oxygenates were also formed. In contrast, the INO-derived electrocatalysts exhibited the unique ability of reducing CO_2 to C_{3+} hydrocarbons and up to C_4 oxygenates (**Extended Data Table 2**). The possible presence of Cu impurities in the Ni samples was ruled out by elemental analyses using inductively coupled plasma optical emission spectrometry (ICP-OES), X-ray photoelectron spectroscopy (**Supplementary Fig. 17**), and energy-dispersive X-ray spectroscopy (**Supplementary Fig. 18**).

Insights into the nature of active sites

To provide insights into the nature of the active sites responsible for C_{2+} hydrocarbon selectivity on our INO-derived electrocatalysts, we first compare the chemical and physical properties of various Ni-based materials. A sputter-deposited Ni displaying a highly defective structure as deduced from its lower average Ni coordination number compared to the ideal metallic state (7.5 versus 12.0), yielded a total C_{2+} product FE of only 2.2%, which is ~1/7 that of PD-Ni (**Supplementary Fig. 7**). Additionally, density functional theory simulations of a stepped Ni(711) surface showed that this facet ($\Delta E_{*\text{CO on Ni(711)}} = -1.33$ eV) binds CO as strongly as Ni(100) ($\Delta E_{*\text{CO on Ni(100)}} = -1.32$ eV) (**Supplementary Table 4** and **Supplementary Fig. 19**). Both surfaces should, thus, be equally poisoned by CO. These results indicate that under-coordinated Ni sites should negligibly contribute to the formation of multicarbon products from CO_2RR.

Since positive charging (or polarization) of Cu sites in Cu^0 matrices have been claimed to enhance C-C coupling[14,15], we investigate the degree of Ni oxidation in the INO electrodes before and during CO_2RR. The oxidation state of Ni in all freshly-prepared INO is +2, according to X-ray absorption near-edge spectroscopy (XANES, **Supplementary Fig. 6)** and Ni^{2+}/Ni^0 redox transitions observed by cyclic voltammetry[16] (**Fig. 3a**). We then monitored how

the oxidation state of Ni in PD-Ni evolved during CO_2RR at -1.2 V versus RHE using *operando* XANES (**Fig. 3b**). Notably, the absorption of the Ni K-edge indicated the existence of stable $Ni^{\delta+}$ sites. We found, by linear combination fitting of the spectra (**Supplementary Table 5**), that 12.0% of the initial Ni^{2+} remained after 15 min of reaction, with no further decrease until the end of the measurements (35 min). Analysis of the *operando* extended X-ray absorption fine structure (EXAFS) spectra (**Fig. 3c**) enabled us to further link these polarized Ni sites to stable Ni-O bonds. The reduced Ni-O distance compared to that in nickel oxide or nickel phosphate suggests the presence of (near-)surface oxygenated species[17,18]. Similar results were also obtained from measurements performed on the nickel borate-derived catalyst (**Supplementary Fig. 20**). These observations point to a key structural difference between oxidic Ni and Cu systems, i.e., unlike Ni, inorganic copper oxygenates undergo reduction to metallic Cu during CO_2RR to a full or almost full extent[19].

The contribution of phosphorus in phosphate form (**Supplementary Fig. 21**) to keep Ni polarization was found to be negligible: the concentration of phosphorus in PD-Ni measured using ICP-OES decreased after the prereduction treatment and slowly during CO_2RR, reaching $\sim$1.0 at.% (P/Ni) after prolonged electrolysis (**Supplementary Fig. 22**). This evidence rules out the possibility that nickel phosphate regions not accessible to electrochemical reduction could be the main source of stable $Ni^{\delta+}$ sites measured using *operando* XANES (12.0% Ni^{2+}). As for the Ni content, modest leaching was observed (**Supplementary Table 6**), possibly due to the insufficient adherence of the catalyst to the gas diffusion layer, which points to the need of developing anchoring strategies for performance optimization.

Mechanistic differences between copper- and nickel-based systems

We now probe the adsorption properties of the nickel catalysts by CO stripping voltammetry. Pristine Ni disc, s-Ni, and commercial NiO (c-NiO) were respectively measured as representative samples of metallic Ni sites, under-coordinated metallic Ni sites, and Ni sites

fully coordinated with oxygen. We discovered that the adsorption strength of CO strongly depends on the nature of the Ni sites. Pristine Ni showed a sharp CO stripping peak centered at 0.54 V versus RHE (**Fig. 4**) due to the strong adsorption of CO (for Ni(100), $\Delta E_{*CO} = -1.32$ eV, **Supplementary Table 7**). The adsorption strength increased on under-coordinated Ni (see s-Ni, peak at 0.54-0.9 V versus RHE in **Fig. 4**)[20], in line with DFT results on Ni(711) steps ($\Delta E_{*CO} = -1.33$ eV, **Supplementary Table 4**) and coordination-based linear scaling relationships[21,22]. For c-NiO, its similar voltammetric responses in Ar- and CO-saturated electrolytes indicate negligible interactions between CO and Ni sites fully coordinated with oxygen (**Supplementary Fig. 23**), as suggested by endothermic binding of CO on a NiO(100) p(3×3) DFT model ($\Delta E_{*CO} = +0.32$ eV). Interestingly, while the behavior of a freshly prepared nickel phosphate electrode expectedly resembled that of c-NiO, a distinct broader CO stripping peak at a less positive potential region (0.41 V versus RHE) compared to that of the Ni disc emerged on the electrochemically reduced nickel phosphate electrode (**Fig. 4** and **Supplementary Fig. 23**). This feature was retained during 12 h of continuous operation and observed for the entire INO family (**Supplementary Figs. 24** and **25**). We underscore that the different morphologies of the Ni materials might also play a role in determining the features of the CO oxidation peak, as reported on Pt[23]. However, the lack of a systematic assessment of morphological effects on the catalytic performance and of a synthetic route enabling simultaneous control of particle size and polarization for Ni makes it difficult to completely decouple, at present, the effect of polarization from that of particle morphology.

In summary, these observations strongly suggest the presence of moderately-bound CO on Ni$^{\delta+}$ sites[24], as compared to on Ni^0. From this, it is reasonable to consider the INO-derived catalysts to be free from CO poisoning (characteristic of metallic Ni), and which subsequently enables them to reduce adsorbed CO species toward long-chain hydrocarbons[25,26].

Due to its key role as a reaction intermediate, CO is known to outperform CO_2 as a feedstock for producing multicarbon products on Cu-based catalysts[27] (**Supplementary**

Fig. 28). We thus electrochemically reduced CO on PD-Ni to check for any parallelism. Strikingly, the rate of electrocatalytic CO reduction was 2 times lower than that of CO_2RR (**Fig. 5**). Hence, a clear difference between Cu and Ni catalysts emerged at this point, suggesting divergent mechanisms at a very early stage of the CO_2RR. We also tested CH_2O and HCOOH as reactants, since they have been claimed as intermediates for CO_2RR to C_3 and C_4 oxygenates on nickel phosphides[8]. Their use produced multicarbon products with even poorer selectivities and production rates (**Fig. 5** and **Supplementary Fig. 29**). Overall, CO_2 was the best sole feedstock.

Additionally, co-feeding CO or CH_2O to CO_2 dramatically improves formation rates of all the multicarbon products, with a CO_2-CO co-feed displaying the best performance (**Fig. 5**). We underscore that $*CH_2$ is the generally proposed intermediate formed from the electrocatalytic reduction of CH_2O[28,29], and thus suggest that chain coupling occurs via an insertion mechanism where CH_2O-like intermediates act as a source of CH_x moieties. In contrast, co-feeding HCOOH with CO_2 showed a very modest impact, which allows us to rule out formate as a reactive species. All in all, our experiments revealed that intermediates directly accessible from CO_2, CO and CH_2O are key pieces in the reaction mechanism developing on INO-derived electrocatalysts.

Nickel polarization enables C-C coupling

Rooted by the physico-chemical features of PD-Ni and mechanistic insights obtained from the preceding experiments, we now explore the main mechanistic features of a polarized Ni surface *via* DFT. Considering the almost complete removal of phosphorus and the presence of Ni-O bonds, we hypothesized that, upon reduction, anions in the INO leave atom-sized cavities in the Ni matrix, which, in contact with solution, can be partially filled by water

fragments (O or OH). Thus, the incorporation of these (near-)surface oxygens and hydroxyls can sustain the presence of polarized sites during CO_2RR.

Experimentally, the Ni catalysts that drove C_{2+} hydrocarbon formation at significant rates (**Extended Data Table 1**) were synthesized from INOs that have Ni-Ni distances larger than that of s-Ni (**Supplementary Table 8**). Besides, selectivity for C_{2+} hydrocarbons correlates with simulated Ni-Ni distances for bulk Ni(100) and the INOs (d_{Ni-Ni} DFT, optimized with PBE[30], see **Supplementary Fig. 30**). Specifically, the *FE* for C_{2+} hydrocarbons increases to 5% for NiO (d_{Ni-Ni} DFT ~ 3 Å) and plateaus to ~10% for Ni-Ni distances between 3.2 and 3.4 Å. Remarkably, the van der Waals radius for water lies within these values (3.4 Å), thus suggesting possible trapping of atomic oxygen (or hydroxyl) from H_2O into the cavities left by the anions. In fact, density functional theory simulations on strained Ni(100) indicate that *O and *OH adsorption becomes favorable for Ni-Ni distances larger than 2.8 Å (**Supplementary Figs. 30**, **31** and **Supplementary Table 9**). This promoting effect is, though, expected to saturate, since extremely strained configurations exhibit high formation energies. This observation may explain the rather constant C_{2+} hydrocarbons selectivity observed for INO-derived electrocatalysts beyond OD-Ni (**Supplementary Fig. 30**).

With this proposed mechanism for the generation and stabilization of $Ni^{\delta+}$ sites, we designed a model to reproduce different degrees of polarization (**Fig. 6a**). Various oxidation states of Ni (from Ni^0 to Ni^{2+}) were obtained by increasing the number of oxygen atoms surrounding a Ni center in a Ni(100) p(3×3) supercell, with the oxide phase NiO(100) p(3×3) representing the fully oxidized surface. We performed DFT simulations employing the PBE density functional and including dispersion (DFT-D2)[30] and effect of electric potential through the Computational Hydrogen Electrode (CHE)[31].

Overall, our results show that the thermodynamic Linear Scaling Relationships (LSR) reported for *COOH, *CO, and *H adsorption on metals[2,32] can be expanded to include an

additional variable term linearly proportional to the charge q of the surface metal atom and the number of bonds (N_{bonds}) between the intermediates and the surface, N_{bonds} (qLSR formalism, **Supplementary Note 1**, **Supplementary Equations (1)-(4)**, **Supplementary Figs. 32** and **33**, **Supplementary Table 10**). N_{bonds} accounts for both active site coordination (determined by the crystalline facet) and the adsorbate dangling bonds and hence, it determines the binding strength between the surface and intermediate. Purely metallic Ni sites ($q_{Ni} = 0$ $|e^-|$) bind adsorbates with high bond order strongly. In contrast, the adsorption strength of intermediates on polarized sites, ΔE^X (q_{Ni}), presents a positive offset which correlates with the Bader charge of the Ni active site (q_{Ni}) and N_{bonds} (**Equation 1**). As shown in **Supplementary Figs. 34** and **35** for 12 different C_1-C_4 chemicals, nickel polarization, q_{Ni}, weakens the adsorption energy of these species (**Supplementary Table 11**), affecting intermediates with higher bond numbers to a larger extent. We thus prove the validity of the qLSR scheme for the C_1-C_4 species involved in C_1-C_1 and C_3+C_1 couplings, whose optimized adsorption configurations with highlighted number of bonds is reported in **Supplementary Fig. 34**.

$$\Delta E^X\left(q_{Ni}\right) = \Delta E^X\left(q_{Ni}=0 \ |e^-|\right) + q_{Ni} \ N_{bonds} \tag{1}$$

Tests with different density functionals and Hubbard corrections (**Supplementary Figs. 36, 37** and **Supplementary Table 12**) further confirm that these trends also hold for dopants other than atomic oxygen, such as 1 OH- and 2 OH-doped Ni(100) p(3×3). These systems showed similar reactivity as 1 O- and 2 O-doped Ni(100). It is notable that OH doping induces lower polarization to Ni centers, thus leading to stronger binding than O-doped Ni sites (**Supplementary Figs. 38** and **Supplementary Table 13**). In fact, in the presence of a OH dopant, $Ni^{\delta+}$ sites exhibit Bader charges of 0.09 $|e^-|$ and 0.25 $|e^-|$ for 1 OH and 2 OH versus 0.15 $|e^-|$ and 0.40 $|e^-|$ for 1 O and 2 O dopants respectively (**Supplementary Figs. 38**). Since the O-doped model considered in **Fig. 6** covers the widest range of polarization degrees

attainable with both O- or OH-doping, we used these systems to investigate the intrinsic reactivity of the polarized sites.

Aiming to rationalize the performance of the INO-derived electrocatalysts, we applied the qLSR formalism to study two critical processes for the formation of C_{2+} products: CO desorption and C-C coupling. Our simulations link Ni polarization with the presence of sites with moderate CO binding and the formation of C_{2+} compounds to a much larger extent than on s-Ni (**Fig. 4, Extended Data Table 1, Supplementary Fig. 34, Supplementary Table 11**). CO desorption on Ni becomes exothermic if nickel is polarized, becoming more favorable than that on metallic Cu(100) (**Fig. 6b**). Weakening of CO adsorption strength on polarized Ni sites was also confirmed for different adsorption configurations and density functionals (**Supplementary Fig. 36**, **Supplementary Table 12**). The weaker CO binding energy on $Ni^{\delta+}$ sites can be attributed to fewer d-electrons available for backdonation in the Blyholder model[33]. As a representative example of a potential first coupling step, the proton-coupled electron transfer (PCET) assisted $*CH_2 + *COOH$ coupling to form $*OCCH_2$ is thermodynamically favorable at −1.2 V versus RHE (**Fig. 6c**). Whilst this process is only slightly exothermic for metallic Ni, it becomes increasingly favored upon nickel charging ($\Delta E_{OCCH2} = -0.64$ eV on Ni^0 to −3.61 eV on Ni^{2+}). Our model system thus predicts a two-fold effect of polarized Ni sites in enabling coupling steps: mild adsorption of intermediates and improvement of C-C coupling.

Proposed CO₂RR pathways on polarized nickel sites

Efforts to unveil all the active mechanistic pathways occurring on Cu catalysts are still ongoing, and these have been limited to the formation of C_1-C_3 compounds[34-36]. The buildup of long-chain hydrocarbons in our Ni systems suggests an even larger complexity at play. Here, we investigate in detail suitable routes for the first C-C coupling step.

Since CO_2 outperformed CO as feedstock (**Fig. 5**), and they are accepted to be mechanistically linked via $CO_2 \rightarrow$ *COOH $\rightarrow$ *CO regardless of the nature of the catalyst[34], we deduced that *COOH could be the relevant coupling intermediate linked to CO_2. Verifiably, the CO_2-CH_2O feed performed better than the CO-CH_2O feed. Furthermore, since the addition of CO or CH_2O did not trigger changes in the α values compared to that of the pure CO_2 feed (**Supplementary Fig. 39**), we conclude that neither CO nor CH_2O interact directly with the existing adsorbates for C-C coupling. Instead, we propose that the intermediates originating from CO or CH_2O precursors are the ones to undergo C-C bond formation. This is supported by simulations, predicting that *CO electroreduction to *CH and *CH_2 is exothermic by 0.3 and 0.5 eV on $Ni^{\delta+}$ sites, respectively (estimated from ΔE in **Supplementary Figure 34**). As mentioned earlier, *CH_2 has been linked to the electrocatalytic reduction of CH_2O[28,29], since CH_2O protonation and consequent reduction to *CH_2 and H_2O is highly exothermic at cathodic biases ($\Delta E < -1$ eV for $U = -1.2$ V versus RHE and $q_{Ni} < 0.56$ |e⁻|, **Supplementary Fig. 40**). This is also in agreement with the observed formation of C_1 to C_4 hydrocarbons from CH_2O electroreduction (**Supplementary Fig. 2**, **Supplementary Table 14**). This collection of evidence leads us to consider *CH_2 and/or *CH as one of the C-C coupling units and *COOH to be the other on nickel catalysts (**Fig. 7a**). This contrasts with the CO dimerization step enabling C_{2+} formation on copper (**Fig. 7b**)[34].

The favorable routes toward the first C-C coupling on polarized Ni surfaces are presented in **Fig. 7a**. As previously discussed, the proton-coupled electron transfer (PCET) assisted *CH_2 + *COOH coupling to form *$OCCH_2$ is exothermic at −1.2 V versus RHE (**Fig. 6c**) and becomes increasingly favored upon nickel charging. Our model predicts that the alternative and potential-independent *CH_2 + *CO coupling becomes exothermic on nickel sites with Bader charges larger than +0.6 |e⁻|, although it is less favorable than the *CH_2 + *COOH path by more than 1 eV (**Supplementary Fig. 41**). This result explains why the formation rate of

multicarbon products is lower for a CO-CH_2O mixture, as compared to a CO_2-CH_2O feed (**Figs. 5** and **7a**). Furthermore, since *CH + *COOH coupling is only 0.5 eV more endothermic than *CH_2 + *COOH (**Supplementary Fig. 41**), we conclude that both pathways are operational. This is evidenced by the overall lower performance of the CO_2-CH_2O co-feed compared to that of the CO_2-CO co-feed, where only the latter pathway, i.e., the *COOH + *CH_2 coupling step is feasible (**Figs. 5** and **7a**). All in all, a mechanism emerges where the first C-C bond formation on polarized Ni surfaces would proceed via the *CH/*CH_2-*COOH coupling pathway (initiation), followed by subsequent *CH and/or *CH_2 insertions (chain growth steps) to form C_{3+} hydrocarbons.

Regarding these further couplings, C-C bond formation can occur by several complementary paths in reaction networks that can encompass more than 2000 individual elementary steps (up to C_3)[37]. One single product can thus be formed by different paths, each contributing to a different extent depending on the potential and the coverage. As the network grows exponentially, we focus on showing the robustness of the *CH/*CH_2 insertion mechanism towards C_4 hydrocarbons, experimentally detected as both linear and branched products (**Extended Data Table 1**). Specifically, we consider the case of *CH/*CH_2 + oxygen-free C_3 intermediate coupling to investigate the Ni polarization effects on the formation of long-chain hydrocarbons and hydrocarbon isomers. The univocal determination of the competition between linear and branched C_4 hydrocarbons (**Supplementary Note 2**, **Supplementary Fig. 42**) is hindered by their similar DFT formation energies, as shown in **Supplementary Fig. 43**. Nonetheless, the formation of those products from *CH/*CH_2 + *C_3 couplings is increasingly favored by higher Ni polarization (**Supplementary Note 1, Supplementary Fig. 44**). Thus, DFT supports a $Ni^{\delta+}$-driven CH/CH_2 insertion mechanism to generate C_4 hydrocarbons and, in general, this scheme may be extended to any C_{3+} species. *Operando* Raman spectroscopy was attempted to acquire experimental evidence supporting the proposed mechanism (**Supplementary Fig. 45**). However, only Ni-CO bands could be clearly identified, which

highlights the need of further development of *operando* techniques to assess complex intermediates with short lifetimes.

Discussion

We have unveiled that different nickel-based electrocatalysts can reduce CO_2 to long-chain hydrocarbons (C_3 to C_6) under ambient conditions in aqueous solutions. The encouraging results on a NiO electrode toward hydrocarbons and oxygenated compounds ($FE_{C2+} = 0.8\%$) were further optimized on other INO-derived electrocatalysts supported on gas diffusion electrodes, which achieved unrivalled *FEs* up to 6.5% toward C_3-C_6 hydrocarbons at −1.2 V versus RHE for at least 12 h of sustained operation.

Operando XANES and EXAFS revealed persistently polarized Ni sites ($Ni^{\delta+}$) during operation as proved by the presence of Ni-O bonds, while CO stripping disclosed the moderate adsorption of CO on its surface. Selected experiments with C_1 reagents disclosed the key role of intermediates directly accessible from CO_2, CO, and CH_2O, evidencing the distinct nature of the mechanisms at work on Cu and Ni systems. The performance variations among the INOs were ascribed to structural variations in the reduced Ni matrix enabling adsorption of oxygen species from water, as supported by DFT simulations. A model nickel surface with different degrees of oxidation served as the basis for DFT simulations that could reconcile experimental observations and enabled a detailed mechanistic description of the first coupling step. Simulations suggest that surface charging is crucial in tuning the adsorption strengths of the intermediates, which is fundamental to allowing Ni to avoid CO poisoning (characteristic of metallic Ni). According to the herein proposed formalism describing Linear Scaling Relations for polarized surfaces (*q*LSR), sites with tunable polarization enable coupling via an insertion mechanism to build the hydrocarbon backbone. We propose that $COOH + CH_x$ ($x = 1, 2$) coupling is the favored C-C dimerization step, in contrast to the widely accepted CO

16

dimerization step on copper, and provide initial evidence supporting further CH/CH_2 insertions toward longer hydrocarbons. Further fundamental and applied studies should be embarked on to explore the envisaged complexity of nickel chemistry. The array of concepts and techniques developed to investigate Cu systems is expected to be of immense value toward this end.

The range of products formed on the nickel-based electrocatalysts expands the scope of CO_2RR studies into the sustainable production of synthetic fuels. As a prospect for practical implementation, the integration of the herein proposed CO_2RR scheme with fuel cells may provide at this seminal stage up to 7% energy efficiency for C_{3+} hydrocarbons (**Supplementary Note 3**, **Supplementary Equations (5)-(7)**, **Supplementary Fig. 46**). This efficiency could be improved by co-feeding CO, either by introducing a separate CO-producing stage or by developing tandem catalysts for direct conversion of CO_2 into CO in the catalytic bed.

Methods

Synthesis of the inorganic nickel oxygenates

Vulcan XC 72 (Cabot Corporation, **Supplementary Fig. 47**) was used as a support to prevent the aggregation of the inorganic nickel oxygenates. For the preparation of nickel phosphate, 100 mg of Vulcan XC 72 was dispersed in 20 mL of an aqueous solution containing 237.7 mg of $NiCl_2 \cdot 6H_2O$ (99.9% trace metals basis, Sigma-Aldrich) and 272.2 mg of KH_2PO_4 ($\geq$ 99.0%, Sigma-Aldrich) under stirring (1000 rpm). After 30 min, 10 mL of 0.1 M KOH (99.99% trace metals basis, Sigma-Aldrich) was added into the mixture. After stirring for another 10 min, the solid was washed three times with 150 mL of ultrapure H_2O (18.2 MΩ) and once with 50 mL of methanol. The solid was redispersed into 10 mL of methanol for further use.

Nickel carbonate, nickel borate, nickel bicarbonate, and nickel hydroxide were synthesized through a similar procedure. Taking the synthesis of nickel carbonate as an example, 100 mg of Vulcan XC 72 was dispersed in 20 mL of aqueous solution containing $NiCl_2 \cdot 6H_2O$ (237.7 mg) under stirring (1000 rpm). The mixture was stirred for another 30 min followed by the addition of 10 mL of 0.1 M K_2CO_3 (99.0% trace metals basis, Sigma-Aldrich). After stirring for 10 min, the solid was washed three times with 150 mL of ultrapure water, and once with 50 mL of methanol. The solid was redispersed into 10 mL of methanol for further use. Synthesis of nickel borate, nickel bicarbonate, nickel hydroxide follows a similar procedure to that of nickel carbonate, except that 0.2 M $Na_2B_4O_7 \cdot 10H_2O$ (99.5%, Sigma-Aldrich), 0.2 M $KHCO_3$ (99.99%, Meryer Chemical Technology Co., Ltd.) and 0.2 M KOH were used respectively instead of 0.1 M K_2CO_3.

Nickel oxide was synthesized by calcinating the nickel hydroxide as prepared through the procedure aforementioned. The as-prepared nickel hydroxide was calcined in a tube furnace under Ar atmosphere at 578 K for 6 h. The nickel oxide sample was collected after being cooled

down to room temperature under Ar flow. X-ray photoelectron spectroscopy (XPS) analysis revealed that the additional thermal procedure did not alter the chemical nature of the carbon support (See **Supplementary Fig. 48**).

Synthesis of sputter-deposited Ni

A gas diffusion layer (Sigracet 38 BC, Fuel cell store) coated with Vulcan XC 72 (0.5 mg cm^{-2}) was used as the substrate for Ni sputtering. Approximately 30 nm thick Ni films were sputtered onto the substrate using a Ni target (99.99%, Chemicals Testing & Calibration Laboratory) at a sputtering rate of ~3 nm min^{-1} in a Discovery®-18 sputtering system at a base pressure of < 10^{-6} Torr.

Synthesis of NiO/Ni

The NiO/Ni samples were prepared in two sequential steps[38,39]. Metallic Ni was firstly deposited onto a freshly polished Ni disc from 50 mL of 0.1 M phosphate buffer solution (pH = 4) containing 2.0 mM $Ni(NO_3)_2 \cdot 6H_2O$ (99.999% trace metals basis, Sigma-Aldrich) by applying a potential of –1.0 V versus Ag/AgCl for 6 min. The passivation of the metallic Ni was performed in 0.1 M phosphate buffer (pH = 7) by using cyclic voltammetry with an applied potential window of –0.5 V to 1.0 V versus Ag/AgCl for 10 cycles at a scan rate of 200 mV s^{-1}.

Preparation of working electrodes

The catalyst ink was prepared by adding 20 μL of Nafion 117 solution (~5wt.% in a mixture of lower aliphatic alcohols and water, Sigma-Aldrich) into 1 mL of the sample dispersion in methanol. The well-mixed catalyst ink was coated onto a 2 cm × 4 cm gas diffusion layer (Sigracet 38 BC, Fuel cell store) by airbrushing with N_2 as a carrier gas. After drying at room temperature overnight, a 2 cm × 2 cm of the as-prepared gas diffusion electrode was assembled into a flow cell electrolyzer for electrocatalytic CO_2 reduction performance test. The working area of the electrode is 1 cm^2. As for the sputter-deposited Ni sample, a 2 cm ×

2 cm sputter-deposited Ni gas diffusion electrode was used. The electrodes for CO-stripping experiments were prepared by drop-coating 30 µL of the catalyst ink on a graphite electrode (15 mm in diameter).

To prepare the ink for the Cu gas diffusion electrode, 6.4 mg of Cu nanoparticles (25 nm, Sigma-Aldrich) (**Supplementary Fig. 49**), 10 mg of Vulcan XC 72, and 20 µL of Nafion 117 solution were dispersed in 1 mL methanol. The Cu gas diffusion electrode was prepared by coating the ink using airbrushing with N_2 as a carrier gas.

Characterization

X-ray diffraction (XRD) patterns were collected on a D8 Advanced Powder Diffractometer (Bruker) with a K_{a1} germanium monochromator for Cu radiation ($\lambda = 1.5406$ Å). X-ray photoelectron spectroscopy (XPS) measurements were carried out on a XPS spectrometer (Thermo ESCALab 250i-XL and Thermo-Scientific Theta Probe spectrometer) using Al K_a X-ray radiation (1.486.6 eV). Carbon C1s at the position at 284.6 eV was used as a reference to correct the charging effect. X-ray absorption measurements at the Ni K-edge were performed at the XAFCA facility in Singapore Synchrotron Light Source (SSLS). An IFEFFIT package was employed to analyze the X-ray absorption spectroscopy (XAS) data[40]. Fourier-transform infrared spectroscopy (FTIR) spectra were collected on a Bruker Alpha spectrometer. Raman spectroscopy was performed using a Raman microscope (LabRAM HR Evolution, Horiba Scientific) with a He-Ne laser ($\lambda = 633$ nm). Scanning electron microscopy (SEM) was performed on a field-emission SEM (JEOL JSM-7600F and FEI Verios 460). Inductively coupled plasma optical emission spectrometry (ICP-OES) was carried out on a Perkin Elmer Avio 500 Inductively Coupled Plasma-Optical Emission Spectrometer. Gas chromatography-mass spectrometry (Shimadzu GCMS-QP2020) was used to distinguish the straight and branched hydrocarbons.

CO stripping measurements

0.1 M KHCO$_3$ was used as the electrolyte for CO stripping experiments. The electrodes were firstly reduced at –1.0 V versus RHE for 10 min under Ar (15 standard cubic centimeter per minute, SCCM) in a H-type cell. The CO was adsorbed onto the working electrode by continuously flowing CO (99.97%, Linde Gas Singapore Pte. Ltd.) into the cell at a flow rate of 15 SCCM for 10 min, while holding the potential at –0.8 V or –0.6 V versus RHE. The gas was subsequently switched to Ar for 10 min to purge CO traces from the working electrode compartment. Cyclic voltammetry was then carried out by sweeping the potential from 0 to 1.0 V versus RHE at 50 mV s^{-1}.

A freshly polished Ni disc, commercial NiO (c-NiO) (**Supplementary Fig. 49**), and sputter-deposited Ni gas diffusion electrode were measured as references.

Electrochemical active surface area (ECSA) measurement

Two methods were used to estimate the ECSA of the electrodes. In the first method, the double-layer capacitance of the as-prepared electrodes was measured in Ar-purged 0.1 M KHCO$_3$. The scan rate varied from 1 to 10 mV s^{-1} in a non-Faradaic potential region. The relative surface areas of the electrodes with respect to the gas diffusion layer were calculated by obtaining the corresponding ratios between double-layer capacitance values. In the second method, the ECSA of Ni was measured based on the reduction of β-NiOOH in an alkaline environment[41]. Cyclic voltammetry curves from –0.3 to 0.7 V (versus Hg/HgO) at a scan rate of 100 mV s^{-1} in Ar-purged 0.1 M KOH were acquired. The ECSA of Ni was calculated based on the reduction peak area of β-NiOOH (100th cycle). The charge required for the oxidation of a smooth Ni surface is taken to be 420 μC cm^{-2}, Ref. [42].

Electrocatalytic reduction of CO$_2$

CO$_2$ electroreduction experiments were conducted using a three-electrode flow cell using a Gamry Reference 3000 potentiostat/galvanostat/ZRA. An anion exchange membrane (AMV, AGC Asahi Glass) was used to separate the cathodic and anodic compartments. The as-

prepared gas diffusion electrode, Ag/AgCl (saturated KCl), and Pt foil were used as the cathode, reference electrode and anode. 0.1 M KHCO$_3$ electrolyte was circulated through the electrochemical cell using a peristaltic pump. Chelex® 100 (100 mesh, Sigma-Aldrich) was used to purify all the electrolytes of possible trace metal contaminants. The gaseous CO$_2$ (99.999%, Linder Gas) passed through the gas chamber with a flow rate of 5 SCCM. The applied potentials were corrected using post-measurement iR drop correction with the uncompensated resistance (R_u) of 86 ohm measured by electrochemical impedance spectroscopy (EIS) at 1.0 MHz. Before CO$_2$ electroreduction, the cathode was pre-reduced at –1.2 V versus RHE for 1 min with CO$_2$ flow. The gas products during the 5000 s electrocatalysis period were analyzed by an on-line gas chromatograph (Shimadzu GC2014) equipped with one thermal conductivity detector and two flame ionization detectors. Calibration plots used for each detected product are provided in **Supplementary Fig. 50**. The liquid products in the electrolyte were analyzed post-CO$_2$RR using a headspace-gas chromatograph (Agilent, 7890B and 7697A) with a flame ionization detector and high-performance liquid chromatography (Agilent 1260 Infinity). The amount of each product was calculated by subtracting the values from control experiments (**Supplementary Table 15**).

Electrocatalytic reduction of C$_1$ compounds

The C$_1$ compounds reduction experiments on gas diffusion electrodes were performed in a three-electrode flow cell. Considering the poor stability of formaldehyde (CH$_2$O) in alkaline conditions, 0.1 M KH$_2$PO$_4$ (pH = 4.6) was used as the electrolyte. Before the experiments, the cathode was pre-reduced using –1.2 V versus RHE for 1 min in 0.1 M KHCO$_3$ with CO$_2$ flow. The electrolyzer was then quickly flushed with the 0.1 M KH$_2$PO$_4$ to remove the possible residual KHCO$_3$ solution and with the subsequent filling of the electrolyte containing different intermediate(s). An applied potential of –1.2 V versus RHE was used. The gas flow rate for all the cases was 5 SCCM, except for the case of CO$_2$-CO in which the total gas flow rate was

10 mL (5 SCCM for CO_2 and CO, respectively). Additional experiments with constant total gas flow (2.5 SCCM for CO_2 and CO, respectively) are shown in **Supplementary Fig. 51**, confirming the same trends. In the cases without CO_2 or CO gas, Ar (99.999%, Chem-Gas) with a gas flow rate of 5 SCCM was used instead. The concentrations of the liquid reactants are 0.04 M for CH_2O and 0.04 M for formic acid. The C_1 intermediates reduction experiments on Cu gas diffusion electrodes were performed in 0.1 M KH_2PO_4 at -1.0 V versus RHE.

Density functional theory modeling

Density functional theory (DFT) was applied through the Vienna Ab Initio Simulation Package (VASP)[43,44], with PBE as density functional[30] and van der Waals dispersion introduced through the DFT-D2 method[45,46], with our reparametrized C_6 coefficients[47]. PAW was employed to represent inner electrons[48,49] and the monoelectronic states corresponding to valence electrons were expanded as plane waves with a kinetic energy cutoff of 450 eV. To address the role of nickel polarization, we modeled the catalysts as Ni(100) p(3×3) doped with (near-)surface oxygen atoms, which we fixed in 1 to 4 hollow sites around the nickel center where intermediates are adsorbed. As metallic references, we considered Ni(100) p(3×3) and Cu(100) p(3×3), the state-of-the-art catalyst for C-C coupling so far[25]. For the most oxidized system, we took the rock-salt structure, antiferromagnetic NiO(100) p(3×3), so that nickel charge could be extended to Ni^{2+} oxidation state[50]. To properly reproduce NiO electronic properties, we applied a Hubbard correction $U_{eff} = 5.3$ eV $= U - J$, with $J = 1$ eV, which are values typically found in literature[50-52]. The validity of this choice was verified upon the exploration of different Hubbard correction values for NiO(100) and polarized Ni sites (**Supplementary Fig. 37**). All simulations related to Ni, O-doped Ni, and NiO were spin-polarized. All the employed slabs contained four layers, with the two outermost relaxed and the rest fixed to the bulk distances. Vacuum thickness between periodic repetitions of the slabs accounted for at least 12 Å. We sampled the Brillouin zone by a Γ-centered k-points mesh from

the Monkhorst-Pack method[53], with a reciprocal grid size smaller than 0.03 Å^{-1}. Each selected C_1-C_4 intermediate and H was placed on Ni^0, $Ni^{\delta+}$, or Ni^{2+} sites to assess the influence of active site polarization on its binding energy. Since adsorption was limited to one side of the periodic cell, we imposed a dipole correction to correct artifacts from the asymmetric slab model[54]. We reported all formation and adsorption energies using the following as energy references: $CO_2(g)$, $H_2(g)$, and the clean surface, either Ni(100), O-doped Ni(100), NiO(100), or Cu(100). We followed the Computational Hydrogen Electrode (CHE) formalism to define the relative energy between the H^+ and the $H_2(g)$ at $U = 0$ V and standard conditions and to correct formation energies for the contribution of electric potential in the case of proton-coupled electron transfer (PCET) steps[27, 31]. Computational details and structural parameters for the DFT simulations can be consulted in the ioChem-BD database (60) in Ref. [55].

Data availability

Experimental data corresponding to the figures and tables of the manuscript is available online in the Zenodo repository under DOI: 10.5281/zenodo.6331376. The DFT datasets generated during the current study are available in the ioChem-BD database (60) at DOI 10.19061/iochem-bd-1-200 (Ref. [55]). All other raw data are available from the corresponding authors upon reasonable request.

**Correspondence and requests for materials** should be addressed to N.L., J.P.R. or B.S.Y.

Author contributions

BSY and JPR coordinated the project. YZ designed the experiments and analyzed the results. FD and NL carried out the computational simulations. AJM assisted the CO-stripping experiments and developed the concept of process integration. SX assisted in conducting the XAFS measurements. All authors read and commented on the manuscript.

## Competing interests

There are no competing interests to declare.

Figures
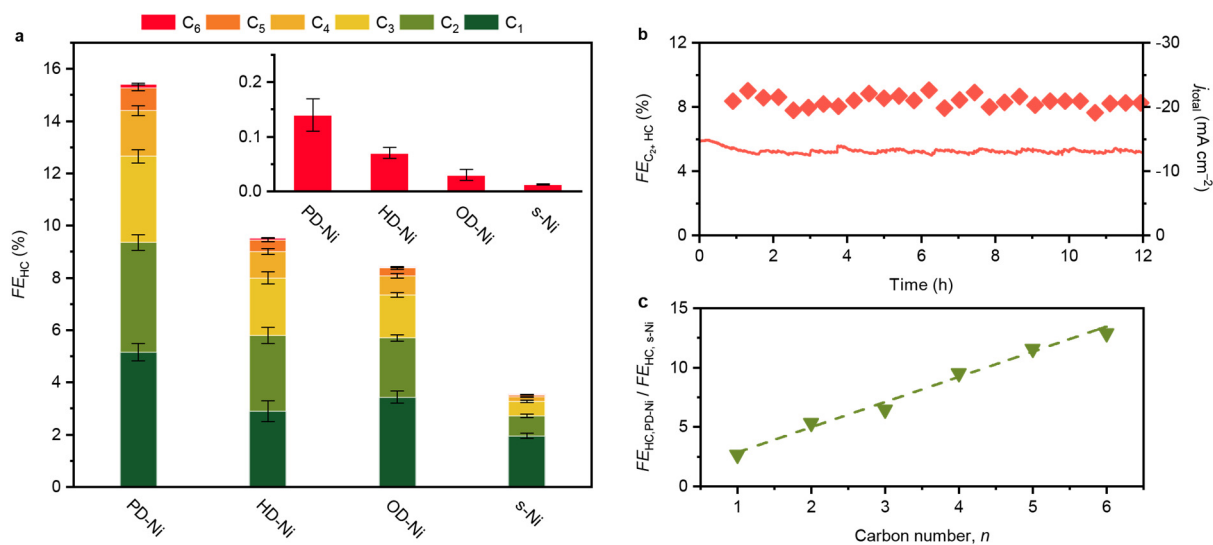
Fig. 1. CO₂ electroreduction to hydrocarbons on Ni catalysts. a, Faradaic efficiencies (*FE*) of C_1-C_6 hydrocarbons formed on sputter-deposited Ni (s-Ni) and selected Ni electrocatalysts derived from nickel phosphate (PD-Ni), nickel hydroxide (HD-Ni) and Ni oxide (OD-Ni) (~1.4 h of electrolysis). Inset shows the *FE* towards C_6 hydrocarbons. Full product distributions are available in **Extended Data Table 1**. **b**, Stability of the PD-Ni catalyst. **c**, Ratio of the *FE* of hydrocarbons on PD-Ni to that on s-Ni versus the carbon number. The dashed line is included to guide the eye. Reaction conditions: 0.1 M KHCO₃ electrolyte was used; –1.2 V versus RHE was applied; measurements were made in a flow cell. HC = hydrocarbon; *j* = current density. The data of OD-Ni was collected after 6 h due to its slow catalyst equilibration to reach stable C_{2+} hydrocarbon *FE*. Error bars represent the standard deviation of three independent measurements for a catalyst.
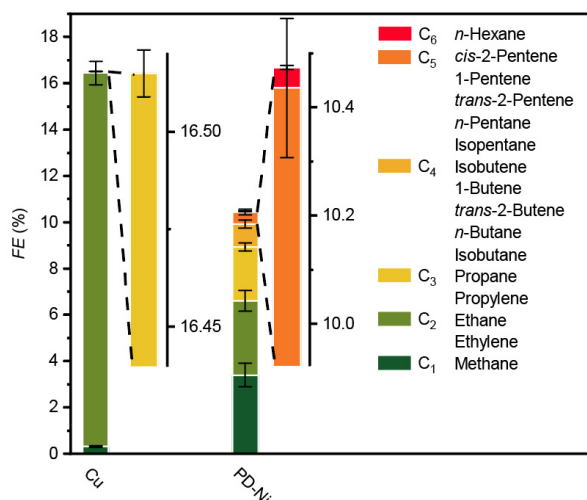
Fig. 2. Hydrocarbons formation on Cu and PD-Ni. Hydrocarbon distribution for Cu and PD-Ni grouped by carbon number. Full product distributions are provided in **Extended Data Table 2**. Reaction conditions: 0.1 M KHCO$_3$ electrolyte was used; –1.0 V versus RHE was applied; measurements were made in a flow cell. Error bars represent the standard deviation of three independent measurements for a catalyst.
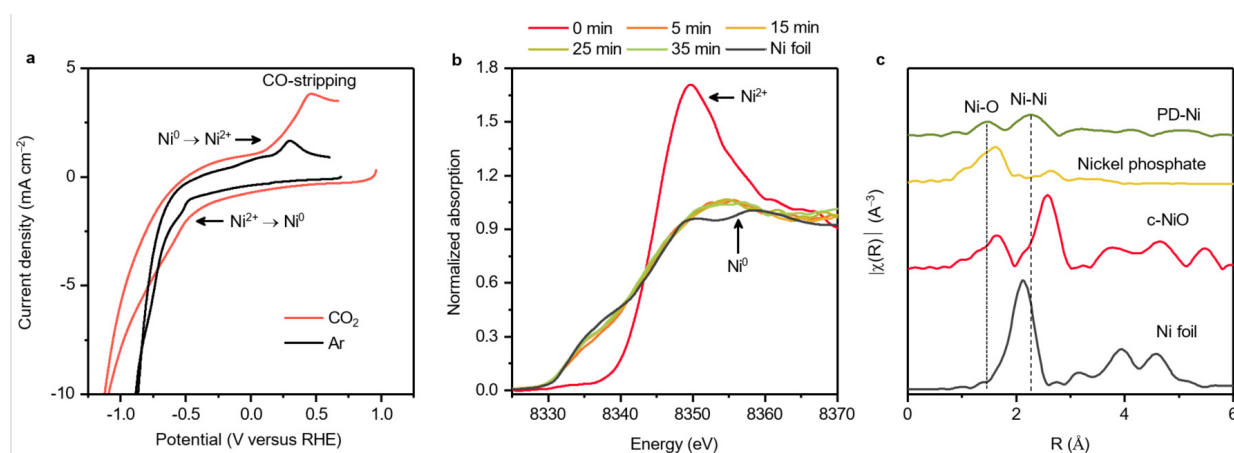

Fig. 3. Redox response and *operando* X-ray absorption spectroscopy studies. a, Cyclic voltammograms of nickel phosphate under Ar and CO$_2$ atmosphere in 0.1 M KHCO$_3$ electrolyte. Scan rate = 20 mV s^{-1}. **b**, *Operando* Ni K-edge XANES spectra of nickel phosphate collected at different times at –1.2 V versus RHE in 0.1 M KHCO$_3$ electrolyte. A Ni foil was

used as a reference for Ni^0 state. **c,** *Operando* Ni K-edge EXAFS spectrum acquired after 35 min under CO_2RR conditions at –1.2 V versus RHE in 0.1 M $KHCO_3$ electrolyte.
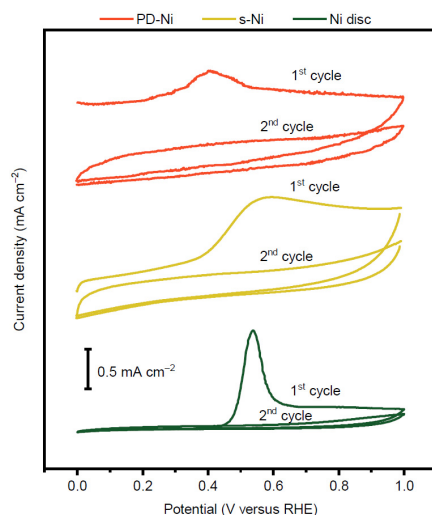

Fig. 4. CO adsorption properties for metallic nickel, s-Ni and PD-Ni catalysts. CO stripping curves on a Ni disc, s-Ni and PD-Ni electrode. CO adsorption was performed at –0.8 V versus RHE. See **Supplementary Fig. 25** for the other Ni compounds. Cyclic voltammograms under CO flow and in CO-saturated 0.1 M $KHCO_3$ electrolyte were also collected to rule out the influence of CO traces after purging (**Supplementary Fig. 26**). Additionally, CO stripping curves were measured after CO adsorption at a more positive potential of −0.6 V versus RHE, so as to reduce the influence of CO reduction (**Supplementary Fig. 27**).
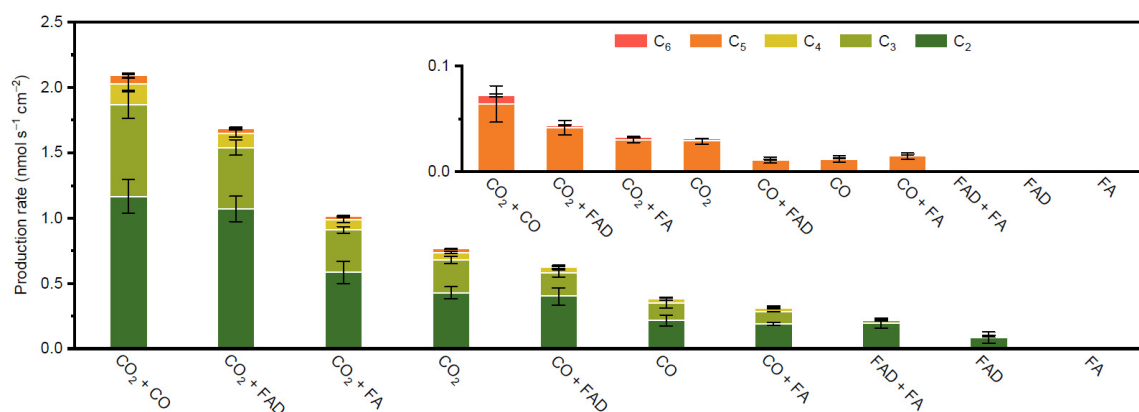

Fig. 5. Experimental screening of key intermediates in the CO_2RR mechanism on PD-Ni. Electrocatalytic reduction of selected C_1 compounds to all the multicarbon products on PD-Ni electrode (C_5 and C_6 production rates in the inset). Reaction conditions: 0.1 M KH_2PO_4 electrolyte was used; –1.2 V versus RHE was applied; measurements were made in a flow cell.

FA = HCOOH, FAD = CH2O. Error bars represent the standard deviation of three independent measurements for an electrode.
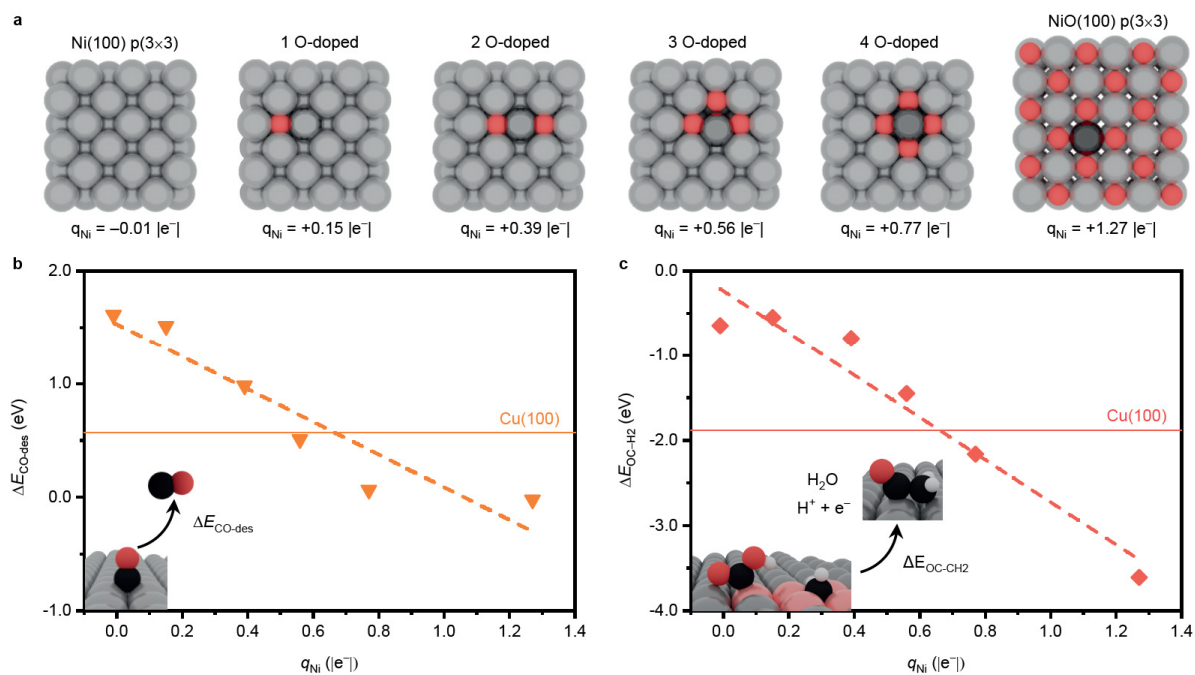
Fig. 6. Impact of Ni polarization on adsorption and insertion steps. a, Top view for Ni(100) p(3×3), (1-4) O-doped Ni(100) p(3×3), and NiO(100) p(3×3) supercells. q_{Ni} represents the Bader charge of the selected adsorption site in units of elementary charge ($|e^-| = 1.6022 \times 10^{-19}$ C). The color of the adsorption site varies from light to dark gray for Ni^0, $Ni^{\delta+}$, or Ni^{2+} respectively. **b**, CO desorption energy versus polarization of Ni adsorption sites. **c**, OCCH2 formation energy via *CH2-*COOH coupling versus polarization of Ni adsorption sites at

29

$U = -1.2$ V versus RHE. Values for Cu(100) are shown as references (solid lines). The dashed lines are drawn to guide the eye.
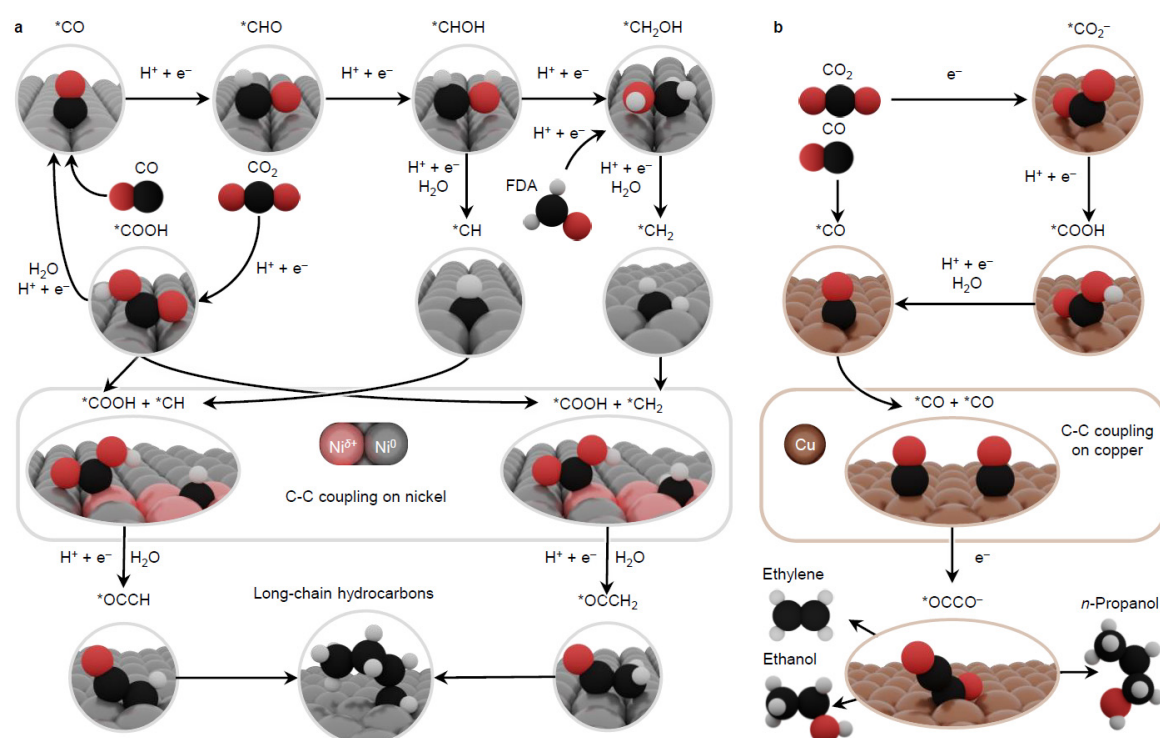
Fig. 7. First C-C coupling steps in the CO$_2$RR on polarized nickel and copper surfaces. a, Initial steps for C-C coupling toward long-chain hydrocarbons on polarized nickel sites. The insertion mechanism, schematically depicted at the bottom of the figure, is expected to sustain the production of C$_{3+}$ products. **b,** Accepted first C-C coupling mechanism on copper, where CO dimerization is the rate-determining step for C$_{2+}$ formation toward the main products ethylene, ethanol and *n*-propanol[34].

References

1   Galán-Martín, Á. *et al.* Sustainability footprints of a renewable carbon transition for the petrochemical sector within planetary boundaries. *One Earth* **4**, 565-583 (2021).

2   Bagger, A., Ju, W., Varela, A. S., Strasser, P. & Rossmeisl, J. Electrochemical CO_2 reduction: A classification problem. *ChemPhysChem* **18**, 3266-3273 (2017).

3   Garcia de Arquer, F. P. *et al.* CO_2 electrolysis to multicarbon products at activities greater than 1 A cm^{-2}. *Science* **367**, 661-666 (2020).

4   Li, F. *et al.* Molecular tuning of CO_2-to-ethylene conversion. *Nature* **577**, 509-513 (2020).

5   Chen, X. *et al.* Electrochemical CO_2-to-ethylene conversion on polyamine-incorporated Cu electrodes. *Nat. Catal.* **4**, 20-27 (2020).

6   Wang, X. *et al.* Efficient electrically powered CO_2-to-ethanol via suppression of deoxygenation. *Nat. Energy* **5**, 478-486 (2020).

7   Torelli, D. A. *et al.* Nickel–gallium-catalyzed electrochemical reduction of CO_2 to highly reduced products at low overpotentials. *ACS Catal.* **6**, 2100-2104 (2016).

8   Calvinho, K. U. D. *et al.* Selective CO_2 reduction to C_3 and C_4 oxyhydrocarbons on nickel phosphides at overpotentials as low as 10 mV. *Energy Environ. Sci.* **11**, 2550-2559 (2018).

9   Kudo, A., Nakagawa, S., Tsuneto, A. & Sakata, T. Electrochemical reduction of high pressure CO_2 on Ni electrodes. *J. Electrochem. Soc.* **140**, 1541-1545 (1993).

10   Hori, Y., Wakebe, H., Tsukamoto, T. & Koga, O. Electrocatalytic process of CO selectivity in electrochemical reduction of CO_2 at metal electrodes in aqueous media. *Electrochimi. Acta* **39**, 1833-1839 (1994).

11   Lee, S., Kim, D. & Lee, J. Electrocatalytic production of C_3-C_4 compounds by conversion of CO_2 on a chloride-induced bi-phasic Cu_2O-Cu catalyst. *Angew. Chem.*

Int. Ed. **127**, 14914-14918 (2015).

12   Bohra, D., Chaudhry, J. H., Burdyny, T., Pidko, E. A. & Smith, W. A. Modeling the electrical double layer to understand the reaction environment in a CO_2 electrocatalytic system. *Energy Environ. Sci.* **12**, 3380-3389 (2019).

13   Hori, Y., Murata, A. & Takahashi, R. Formation of hydrocarbons in the electrochemical reduction of carbon dioxide at a copper electrode in aqueous solution. *J. Chem. Soc., Faraday Trans. 1* **85** (1989).

14   Xiao, H., Goddard, W. A., Cheng, T. & Liu, Y. Cu metal embedded in oxidized matrix catalyst to promote CO_2 activation and CO dimerization for electrochemical reduction of CO_2. *Proc. Natl. Acad. Sci. U.S.A.* **114**, 6685-6688 (2017).

15   Arán-Ais, R. M., Scholten, F., Kunze, S., Rizo, R. & Roldan Cuenya, B. The role of in situ generated morphological motifs and $Cu_{(I)}$ species in C_{2+} product selectivity during CO_2 pulsed electroreduction. *Nat. Energy* **5**, 317-325

16   Huang, L. F., Hutchison, M. J., Santucci, R. J., Scully, J. R. & Rondinelli, J. M. Improved electrochemical phase diagrams from theory and experiment: The Ni–water system and its complex compounds. *J. Phys. Chem. C* **121**, 9782-9789 (2017).

17   Stohr, J. *et al.* Extended absorption fine structure studies above the carbon, nitrogen, oxygen, and fluorine K absorption edges. *Appl. Opt.* **19**, 3911-3919 (1980).

18   Stöhr, J. Surface EXAFS studies using electron yield spectroscopy: Oxygen on Ni (100). *Jpn. J. Appl. Phys.* **17** (1978).

19   Nitopi, S. *et al.* Progress and perspectives of electrochemical CO_2 reduction on copper in aqueous electrolyte. *Chem. Rev.* **119**, 7610-7672 (2019).

20   de Amorim, R. V. *et al.* CO, NO, and SO adsorption on Ni nanoclusters: a DFT investigation. *Dalton Trans.* **49**, 6407-6417 (2020).

21   Calle-Vallejo, F., Martinez, J. I., Garcia-Lastra, J. M., Sautet, P. & Loffreda, D. Fast

prediction of adsorption properties for platinum nanocatalysts with generalized coordination numbers. *Angew. Chem. Int. Ed.* **53**, 8316-8319 (2014).

22   Pérez-Ramírez, J. & López, N. Strategies to break linear scaling relationships. *Nat. Catal.* **2**, 971-976 (2019).

23   Mayrhofer, K. J. J. *et al.* CO surface electrochemistry on Pt-nanoparticles: A selective review. *Electrochim. Acta* **50**, 5144-5154 (2005).

24   Rudi, S., Cui, C., Gan, L. & Strasser, P. Comparative study of the electrocatalytically active surface areas (ECSAs) of Pt alloy nanoparticles evaluated by H_{upd} and CO-stripping voltammetry. *Electrocatalysis* **5**, 408-418 (2014).

25   Birdja, Y. Y. *et al.* Advances and challenges in understanding the electrocatalytic conversion of carbon dioxide to fuels. *Nat. Energy* **4**, 732-745 (2019).

26   Peterson, A. A., Abild-Pedersen, F., Studt, F., Rossmeisl, J. & Nørskov, J. K. How copper catalyzes the electroreduction of carbon dioxide into hydrocarbon fuels. *Energy Environ. Sci.* **3** 1311-1315 (2010).

27   Zhang, H., Li, J., Cheng, M.-J. & Lu, Q. CO electroreduction: Current development and understanding of Cu-based catalysts. *ACS Catal.* **9**, 49-65 (2018).

28   Russell, P. G., Kovac, N., Srinivasan, S. & Steinberg, M. The Electrochemical reduction of carbon dioxide, formic acid, and formaldehyde. *J. Electrochem. Soc.* **124**, 1329-1338 (2019).

29   Liu, X. *et al.* pH effects on the electrochemical reduction of $CO_{(2)}$ towards C_2 products on stepped copper. *Nat. Commun.* **10**, 32 (2019).

30   Perdew, J. P., Burke, K. & Ernzerhof, M. Generalized gradient approximation made simple. *Phys. Rev. Lett.* **77**, 3865-3868 (1996).

31   Nørskov, J. K. *et al.* Origin of the overpotential for oxygen reduction at a fuel-cell cathode. *J. Phys. Chem. B* **108**, 17886-17892 (2004).

32   Abild-Pedersen, F. *et al.* Scaling properties of adsorption energies for hydrogen-

containing molecules on transition-metal surfaces. *Phys. Rev. Lett.* **99**, 016105 (2007).

33   Blyholder, G. Molecular orbital view of chemisorbed carbon monoxide. *J. Phys. Chem.* **68**, 2772-2777 (1964).

34   Kortlever, R., Shen, J., Schouten, K. J., Calle-Vallejo, F. & Koper, M. T. M. Catalysts and reaction pathways for the electrochemical reduction of carbon dioxide. *J. Phys. Chem. Lett.* **6**, 4073-4082 (2015).

35   Handoko, A. D., Wei, F., Jenndy, Yeo, B. S. & Seh, Z. W. Understanding heterogeneous electrocatalytic carbon dioxide reduction through operando techniques. *Nat. Catal.* **1**, 922-934 (2018).

36   Garza, A. J., Bell, A. T. & Head-Gordon, M. Mechanism of CO_2 reduction at copper surfaces: Pathways to C_2 Products. *ACS Catal.* **8**, 1490-1499 (2018).

37   Pablo-García, S. *et al.* Mechanistic routes toward C3 products in copper-catalysed CO2 electroreduction. *Catal. Sci. Technol.* **12**, 409-417 (2022).

38   Abd El-Lateef, H. M., Almulhim, N. F., Alaulamie, A. A., Saleh, M. M. & Mohamed, I. M. A. Design of ultrafine nickel oxide nanostructured material for enhanced electrocatalytic oxidation of urea: Physicochemical and electrochemical analyses. *Colloids Surf., A Physicochem. Eng. Asp.* **585**, 124092 (2020).

39   El-Refaei, S. M., Awad, M. I., El-Anadouli, B. E. & Saleh, M. M. Electrocatalytic glucose oxidation at binary catalyst of nickel and manganese oxides nanoparticles modified glassy carbon electrode: Optimization of the loading level and order of deposition. *Electrochim. Acta* **92**, 460-467 (2013).

40   Ravel, B. & Newville, M. ATHENA, ARTEMIS, HEPHAESTUS: data analysis for X-ray absorption spectroscopy using IFEFFIT. *J. Synchrotron. Radiat.* **12**, 537-541 (2005).

41   Cossar, E., Houache, M. S. E., Zhang, Z. & Baranova, E. A. Comparison of electrochemical active surface area methods for various nickel nanostructures. *J.*

Electroanal. Chem. **870**, 114246 (2020).

42   Ho, J. C. K. & Piron, D. L. Active surface area in oxide electrodes by overpotential deposited oxygen species for the oxygen evolution reaction. *J. Appl. Electrochem.* **26**, 515-521 (1996).

43   Kresse, G. & Furthmüller, J. Efficiency of ab-initio total energy calculations for metals and semiconductors using a plane-wave basis set. *Comput. Mater. Sci.* **6**, 15-50 (1996).

44   Kresse, G. & Furthmuller, J. Efficient iterative schemes for ab initio total-energy calculations using a plane-wave basis set. *Phys. Rev. B* **54**, 11169-11186 (1996).

45   Grimme, S. Semiempirical GGA-type density functional constructed with a long-range dispersion correction. *J. Comput.Chem.* **27**, 1787-1799 (2006).

46   Bucko, T., Hafner, J., Lebegue, S. & Angyan, J. G. Improved description of the structure of molecular and layered crystals: ab initio DFT calculations with van der Waals corrections. *J. Phys. Chem. A* **114**, 11814-11824 (2010).

47   Almora-Barrios, N., Carchini, G., Błońsk, P. & López, N. Costless derivation of dispersion coefficients for metal surfaces. *J. Chem. Theory Comput.* **10**, 5002-5009 (2014).

48   Blochl, P. E. Projector augmented-wave method. *Phys. Rev. B* **50**, 17953-17979 (1994).

49   Kresse, G. & Joubert, D. From ultrasoft pseudopotentials to the projector augmented-wave method. *Phys. Rev. B* **59**, 1758-1775 (1999).

50   Garcés-Pineda, F. A., Blasco-Ahicart, M., Nieto-Castro, D., López, N. & Galán-Mascarós, J. R. Direct magnetic enhancement of electrocatalytic water oxidation in alkaline media. *Nat. Energy* **4**, 519-525 (2019).

51   Rohrbach, A., Hafner, J. & Kresse, G. Molecular adsorption on the surface of strongly correlated transition-metal oxides: A case study for CO/NiO(100). *Phys. Rev. B* **69**,

075413 (2004).

52   Dudarev, S. L., Botton, G. A., Savrasov, S. Y., Humphreys, C. J. & Sutton, A. P. Electron-energy-loss spectra and the structural stability of nickel oxide: An LSDA+U study. *Phys. Rev. B* **57**, 1505-1509 (1998).

53   Monkhorst, H. J. & Pack, J. D. Special points for Brillouin-zone integrations. *Phys. Rev. B* **13**, 5188-5192 (1976).

54   Makov, G. & Payne, M. C. Periodic boundary conditions in ab initio calculations. *Phys. Rev. B* **51**, 4014-4022 (1995).

55   Dattila, F. eFTS nickel. ioChem-BD https://doi.org/10.19061/iochem-bd-1-200 (2021).